ACS OMEGA

Open Access

http://pubs.acs.org/journal/acsodf

Article

Biomimetic Gd−Metal−Organic Framework Radiosensitizer for Near-Infrared Fluorescence Imaging-Guided Radiotherapy toward Nasopharyngeal Carcinoma

Wenlong Lv,[⊥] Yanbin Chen,[⊥] Wencong Hong, Linzhen Lan, Jun Chen, Feibao Guo, and Xi Zou*

Cite This: *ACS Omega* 2024, 9, 38272−38283

Read Online

ACCESS | Metrics & More | Article Recommendations | Supporting Information

ABSTRACT: Radiotherapy (RT) is recognized as a primary treatment modality for Nasopharyngeal carcinoma (NPC). However, enhancing RT's targeting accuracy and selectivity remains a significant challenge. In this study, we present an innovative radiosensitizer, Gd−metal−organic framework (MOF)-based nanocarrier coated with indocyanine green (ICG) and red blood cell membrane (RBCM), designed to bypass immune clearance and achieve prolonged circulation within the bloodstream. This design significantly enhances tumor localization and systemic circulation, as evidenced by in vivo analyses. The strategic accumulation of the Gd-MOF-ICG nanocarrier at the tumor site facilitates precise tumor localization and sensitization to RT, leveraging the RBCM camouflage to enhance the tumor uptake potential. Our comprehensive study introduces a potent approach for optimizing RT in NPC treatment through this advanced theranostic nanoplatform, which combines material science with biomedical engineering to augment the effectiveness of RT and underscores the significance of precision in cancer therapy. This strategy offers a promising avenue for clinical application and further research in targeted cancer treatments.

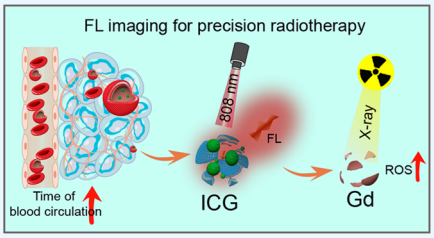

1. INTRODUCTION

Globally, among newly diagnosed cancer patients, those with Nasopharyngeal carcinoma (NPC) account for approximately 0.7%, with the incidence of this disease being primarily influenced by environmental changes and genetic factors.[1] Although NPC exhibits a relatively low incidence, over 80% of patients have a chance of curative treatment, primarily through radiotherapy (RT), which stands as the most critical and widely utilized therapeutic approach for NPC.[1,2] The Gd-MOF-ICG-RBCM nanocomposites enhance radiotherapy by increasing the local radiation dose through the high atomic number of Gd, which improves the absorption of X-rays. This leads to the production of reactive oxygen species (ROS), inducing DNA damage, and enhancing the tumor cell killing effect. High-atomic-number elements, such as gadolinium, absorb the radiation energy and subsequently produce secondary electrons. These secondary electrons interact with water molecules present in the cells, generating hydroxyl radicals and other ROS, which cause oxidative stress and damage to cellular components, particularly DNA. This process enhances the efficacy of radiotherapy by increasing the sensitivity of tumor cells to radiation, thereby reducing the required dose and minimizing damage to surrounding healthy tissues. The primary mechanism by which radiotherapy kills tumor cells is using high-energy ionizing radiation, which either directly damages DNA molecules or interacts with water to generate hydroxyl radicals, leading to cell death.[3] Due to the low selectivity of ionizing radiation,[4] as the sensitivity difference between human normal tissues and cancerous tissues to ionizing radiation is minimal,[5] radiotherapy's selectivity is low, making it extremely prone to inadvertently damaging normal cells.[6]

Additionally, in clinical practice, the inability to precisely locate tumor tissues when irradiating tumors exacerbates the risk of normal tissue exposure to radiation.[7] Therefore, auxiliary imaging methods such as computerized tomography (CT) imaging,[8] magnetic resonance imaging,[9] and ultrasound imaging[10] are needed. However, due to the inability of the aforementioned imaging methods to achieve real-time imaging for precise positioning, there is an urgent need to develop new imaging modalities. Near-infrared second-window imaging,[11] with its deep penetration, real-time imaging, and ease of operation, can precisely locate tumors during radiotherapy, thereby enhancing the precision of radiotherapy and reducing the occurrence of side effects.

Furthermore, high doses of radiation in radiotherapy can also cause patients acute side effects such as nausea, vomiting, and skin burns, as well as chronic side effects like normal tissue fibrosis.[12] Therefore, how to reduce the dosage of radiotherapy to achieve the original therapeutic effect remains a key issue in the treatment of NPC. Introducing radiosensitizers into the

Received: July 4, 2024
Revised: August 16, 2024
Accepted: August 23, 2024
Published: August 28, 2024

https://doi.org/10.1021/acsomega.4c06191
ACS Omega 2024, 9, 38272−38283

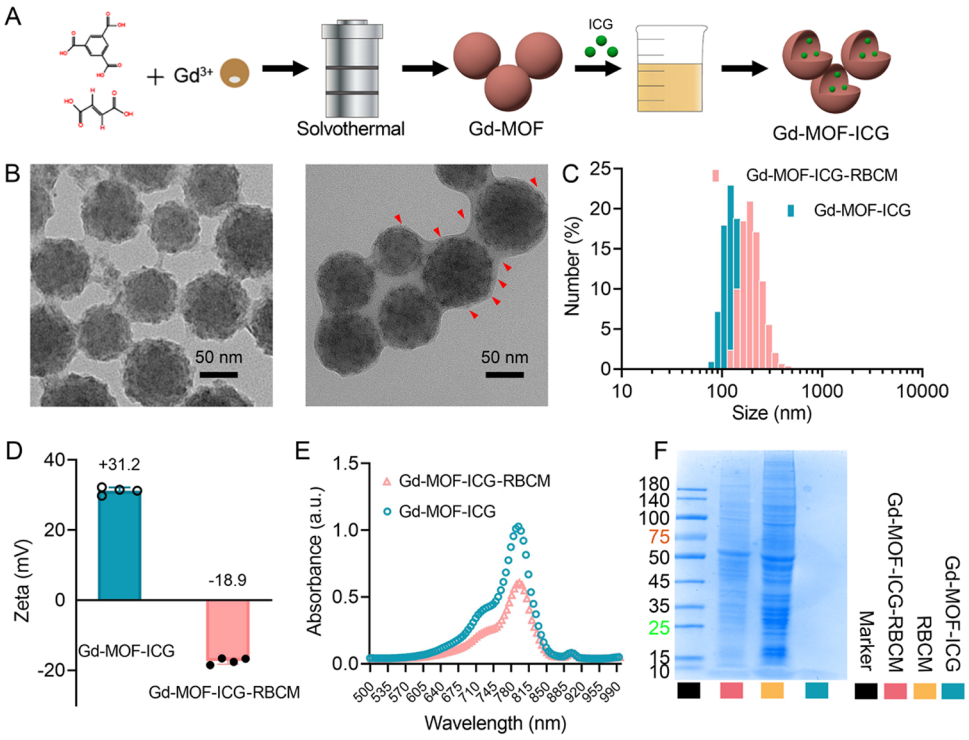

Figure 1. Comprehensively characterization of Gd-MOF-ICG-RBCM nanocarriers. (A) Schematic illustration of Gd-MOF-ICG synthesis: Synthesis steps, including Gd-MOF formation, ICG loading, and RBCM coating for enhanced biocompatibility and circulation. (B) TEM images displaying morphology and structure, highlighting successful RBCM coating. (C) Size distribution: DLS analysis showing an increased particle size after RBCM coating, confirming encapsulation. (D) ζ-Potential Indicating a shift from positive to negative charge upon RBCM coating, showing successful surface modification. (E) UV−vis spectra confirming the presence and stability of ICG within the MOF structure. (F) Coomassie Brilliant Blue staining verifying the presence of RBCM proteins on the nanoparticles, confirming successful coating.

tumor is an effective strategy to selectively increase the sensitivity of tumor cells to radiation, while minimizing the impact on surrounding normal tissues. However, the effects of traditional radiosensitizers, such as misonidazole,[13] cisplatin,[14] fluorouracil,[15] and cysteine derivatives,[13,16] are not ideal. To simultaneously maximize the radiosensitivity of tumor tissues while protecting normal tissue structures, many high-atomic-number element nanoparticles, such as Gd,[17] Hf,[18] Au,[19] and Bi,[20] have been synthesized and applied.

Existing studies have shown that high-atomic-number elements, with more protons and electrons, have a strong absorption capacity for electromagnetic radiation, especially X-rays and γ rays.[18] When irradiated, these atoms can trigger the Compton effect and the photoelectric effect to produce photoelectrons such as Compton electrons and Auger electrons, ultimately inducing cell apoptosis and necrosis.[21] In this context, metal−organic framework (MOF) nanomaterials have attracted researchers' attention due to their unique advantages.[22] MOFs, formed by the self-assembly of metal ions or clusters with organic ligands, not only can integrate a variety of high-atomic-number elements to enhance radiation absorption but also their porous nature greatly enhances their drug-carrying capacity and selective targeting ability.[23] Through their porosity, fluorescent molecules, such as indocyanine green (ICG) and Gd, can be easily integrated into a single dosage form. Among these high-atomic-number-element-based nanomaterials, engineered gold-based radiosensitizers, due to their low toxicity, ease of preparation, and high chemical stability, have been extensively studied for cancer radiotherapy.

We have developed an innovative theranostic nanoplatform guided by near-infrared fluorescence imaging for radiotherapy sensitization, which is camouflaged with a red blood cell membrane and core-composed of porous Gd-MOF (metal−organic framework) nanoparticles, loaded with the near-infrared fluorescent dye ICG, a dye approved by the Food and Drug Administration (FDA) for in vivo application. Designed for systemic administration, this nanosystem, through the camouflage of the red blood cell membrane, effectively reaches the areas of nasopharyngeal cancer and stays there for a long time. After these nanoparticles are taken up by tumor cells, an 808 nm laser can be used for imaging of the tumor site. With the guidance of near-infrared fluorescence imaging technology, precise radiotherapy sensitization is achieved with this platform. Radiotherapy, through high-energy X-rays or γ rays,[23] directly causes the destruction of the molecular structure of DNA in tumor cells, leading to single or double-stranded breaks. The introduction of Gd ions not only enhances the absorption of radiation energy but also promotes the production of secondary electrons, thereby significantly increasing the generation of reactive oxygen species (ROS).[21] ROS, as a key factor in cell damage and death, whose increase exacerbates the oxidative stress in tumor cells, further enhances the lethality of radiotherapy. Additionally, radioactive radiation can produce free radicals through the ionization of water molecules, which react with deoxyribonucleic acid (DNA), causing additional DNA damage. In summary, the theranostic nanoplatform presented in this study demonstrates the following main advantages: (1) The red blood cell membrane camouflage technique significantly prolongs the circulation time of nanomaterials in the body, indirectly increasing the

https://doi.org/10.1021/acsomega.4c06191
ACS Omega 2024, 9, 38272−38283

Scheme 1. (A) Schematic Illustration of Biomimetic Gd-MOF-ICG-RBCM Nanoprobes Synthesis. (B) Mechanism of Radiotherapy Sensitizers (Gd-MOF-ICG-RBCM) Generating ROS and Imaging with Near-Infrared Fluorescence

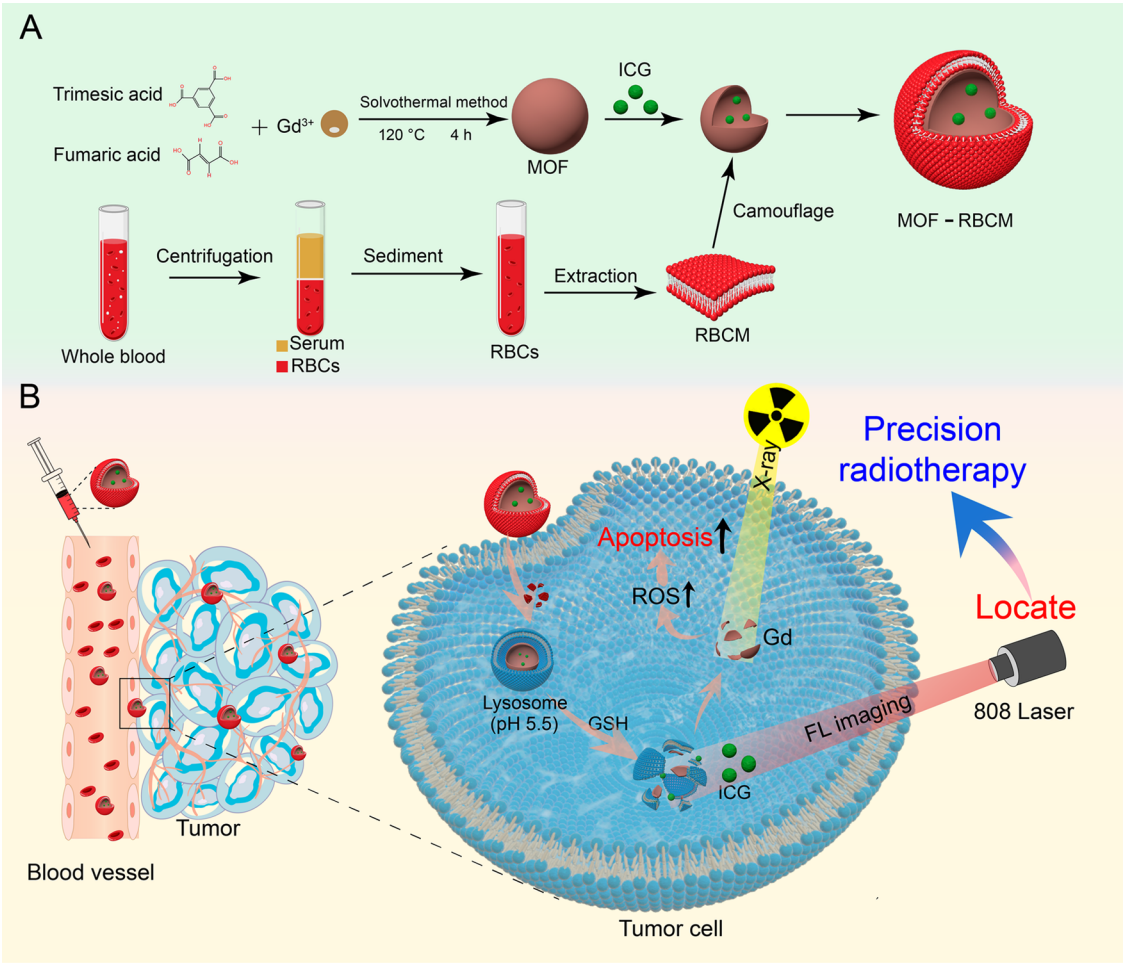

uptake of nanoparticles by tumors; (2) The use of near-infrared fluorescence imaging technology for precise guidance of X-ray radiotherapy improves the accuracy of treatment; (3) The release of ROS by Gd ions stimulated by X-ray radiation significantly enhances the efficiency of killing tumor cells, thereby improving the effects of radiotherapy in vitro and in vivo. This study provides an efficient theranostic strategy for radiotherapy sensitization, demonstrating significant potential for NPC treatment.

2. RESULTS AND DISCUSSION

2.1. Preparation and Characteristics of Gd-MOF-ICG-RBCM. The preparation of the membrane-coated nanomedicine is illustrated in Figure 1A. The construction of the intimal nanomedicine is illustrated through the synthesis process of Gd-MOF-ICG, as shown in Scheme 1. Subsequently, the fresh cell membrane from red blood cell (RBC) was isolated and layered onto the as-prepared nanomedicine surface through repeated extrusion. The morphology and properties of Gd-MOF-ICG-RBCM were examined. Transmission electron microscopy (TEM) images (Figure 1B) highlight uniform porous core−shell sphere structures for Gd-MOF-ICG-RBCM with average particle sizes of 126 ± 3 nm. And a transparent fluctuant surface signified the presence of the RBC membrane on Gd-MOF-ICG-RBCM. Concurrently, dynamic light scattering (DLS) also indicates the presence of the RBCM, as evidenced by the increase in the average hydrodynamic diameter from 110 to 160 nm and the reversal in surface charge from the positive (31.2 ± 0.4 mV) to negative charges (−18.9 ± 0.3 mV) before and after the RBCM coating (Figure 1C,D). The sample of Gd-MOF-ICG-RBCM prepared by lyophilization method was detected by powder X-ray diffractometer. It can be observed that in Figure S1, Gd contains multiple sharp characteristic absorption peaks in the range of Bragg angles from 20 to 40°, indicating the crystal structure of MOF. To analyze the impact of repeated extrusion on the protein components of the RBCM, sodium dodecyl sulfate-polyacrylamide gel electrophoresis (SDS-PAGE) gel analysis was subjected. The result is shown in Figure 1E and revealed that the Gd-MOF-ICG-RBCM boasted most of the proteins of RBCM, important for the function to invade immune cognition effectively. Moreover, spectrum analysis also found that the absorbance profile, with 800 nm of λ_{max} value between 500 and 990 nm, from Gd-MOF-ICG-RBCM was almost consistent with that from the naked-state ICG, indicating the successful encapsulation of ICG (Figure 1F). Collectively, these observations attest to the successful construction of Gd-MOF-ICG-RBCM.

2.2. Radiation Sensitization of Gd-MOF-ICG-RBCM In Vitro. The effectiveness of radiotherapy hinges on the productivity of cytotoxic reactive oxygen species (ROS) (Figure 2A), like hydroxyl radicals ($^{\bullet}$OH), superoxide radicals

https://doi.org/10.1021/acsomega.4c06191
ACS Omega 2024, 9, 38272−38283

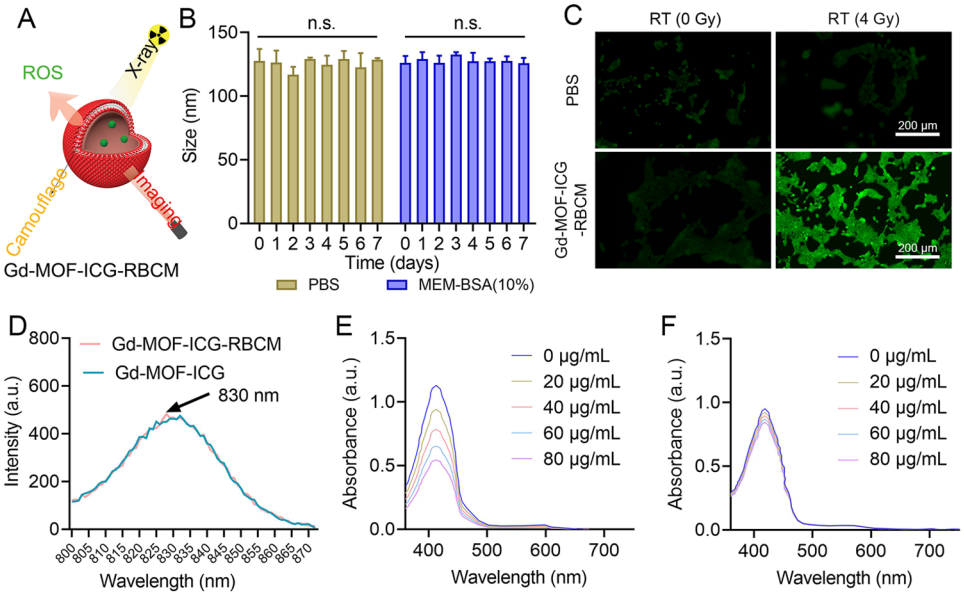

Figure 2. In vitro radiosensitizing impact of Gd-MOF-ICG-RBCM. (A) Schematic diagram of the functionality of nanoparticles. This panel illustrates how Gd-MOF-ICG@RBCM functions as a radiosensitizer. (B) Stability of Gd-MOF-ICG-RBCM in PBS or MEM-BSA (10%). This panel shows the stability of Gd-MOF-ICG@RBCM nanoparticles when suspended in phosphate-buffered saline (PBS) or MEM with 10% bovine serum albumin (BSA) over time. (C) ROS generation in CNE1 tumor cells. Fluorescence images of CNE1 tumor cells stained with DCFH-DA, showing the generation of reactive oxygen species (ROS) upon treatment with Gd-MOF-ICG@RBCM and subsequent X-ray irradiation. (D) Fluorescence spectra of ICG and Gd-MOF-ICG-RBCM. This panel presents the fluorescence spectra of free ICG and Gd-MOF-ICG@RBCM, indicating that the encapsulated ICG retains its optical properties. (E) ROS production detected by DPBF following X-ray irradiation at 4 Gy. The change in absorbance of DPBF, a singlet oxygen sensor, is shown after X-ray irradiation, indicating the generation of ROS by Gd-MOF-ICG@RBCM. (F) ROS production detected by DPBF following X-ray irradiation at 0 Gy: The control experiment showing no significant change in DPBF absorbance without X-ray irradiation, confirming the necessity of X-ray exposure for ROS generation.

(O^{2-}), and singlet oxygen ($^1O_2$), from photosensitizers under radiation.[24] Consequently, the productivity of the ROS attributes of Gd-MOF-ICG-RBCM was scrutinized. In order to exclude the effect of the disintegrated nanostructures on the subsequent detection, the stability of Gd-MOF-ICG-RBCM under different conditions was first explored. Compared to the initial day, a negligible amount of variation in diameter of Gd-MOF-ICG-RBCM was found after storing at PBS or MEM-10% BSA solution for 7 days, implying the maintenance of nanostructures during 7 days under physiological environment (Figure 2B). Next, the generation of ROS by Gd has been ascertained. Given that 1,3-diphenylisobenzofuran (DPBF) interacts with ROS, causing its irreversible oxidation and a dip in its absorption at 410 nm, DPBF is thus feasible to gauge ROS generation. Upon amalgamating DPBF (0.1 mM) with various Gd-MOF-ICG-RBCM concentrations (0−80 ug/mL) and subsequently subjecting them to X-ray exposure (4 Gy), there is a conspicuous reduction tendency of absorption in concentration-dependent behavior, along with a maximum decrease of 25% under 80 ug/mL Gd-MOF-ICG-RBCM (Figures 2C and S2). On the contrary, no significant change in the absorption occurred at any NPs concentration when X-ray did not work (Figure 2D). Moreover, under 4 Gy X-ray irradiation, the intense green fluorescent signal could be observed in CNE1 cells which were pretreated with Gd-MOF-ICG-RBCM and then incubated with DCFH-DA probe (another probe to reveal the presence of intracellular ROS), considerably surpassing its nonirradiated or non-NPs counterpart (Figure 2E). These observations underscore ROS generation prowess of Gd-MOF-ICG-RBCM, which is attributed to concentration and X-ray sensitivity. In addition, to explore whether MOF encapsulation and the cell membrane camouflage would affect the imaging ability of ICG, we compared the fluorescence spectrum between Gd-MOF-ICG-RBCM and free ICG. As shown in Figure 2F, we found a nearly identical fluorescence profile and the same maximum emission wavelengths at 830 nm between them, exhibiting that the Gd-MOF-ICG-RBCM preserved the imaging function from ICG.

2.3. In Vitro Uptake and Radiotherapy. Before exploring the radiosensitizing effects of Gd-MOF-ICG-RBCM on killing cancer cells (Figure 3A), we first assessed the uptake of Gd-MOF-ICG-RBCM by CNE1 cells, using the noncoated nanoparticle Gd-MOF-ICG as a control group treatment. The results showed that the cells, which were cultivated in a medium containing Gd-MOF-ICG-RBCM, reached the highest uptake at 6 h, achieving a dynamic equilibrium, and the cellular intake did not increase after 8 h (Figures 3B and S3−S5). Moreover, the uptake of Gd-MOF-ICG, which was not modified by red blood cell membrane, was less than that of the experimental group, a difference that can be attributed to the negative charge on the nanoparticle surface, which increases cellular uptake, thanks to the camouflage provided by the red blood cell membrane. Subsequently, different concentrations of Gd-MOF-ICG-RBCM were incubated with tumor cells for 6 h, after which the cytotoxicity of cells that were not irradiated with X-rays was essentially negligible (Figure 3C), indicating that Gd-MOF-ICG-RBCM has good biocompatibility and potential for application in NPC treatment.

Then, after cells were incubated with the same concentration of the nanoparticle, radiation experiments were conducted with 2 Gy (Figure 3D) and 4 Gy (Figure 3E) doses. It can be clearly seen from the figures that with the increase in the

https://doi.org/10.1021/acsomega.4c06191
ACS Omega 2024, 9, 38272−38283

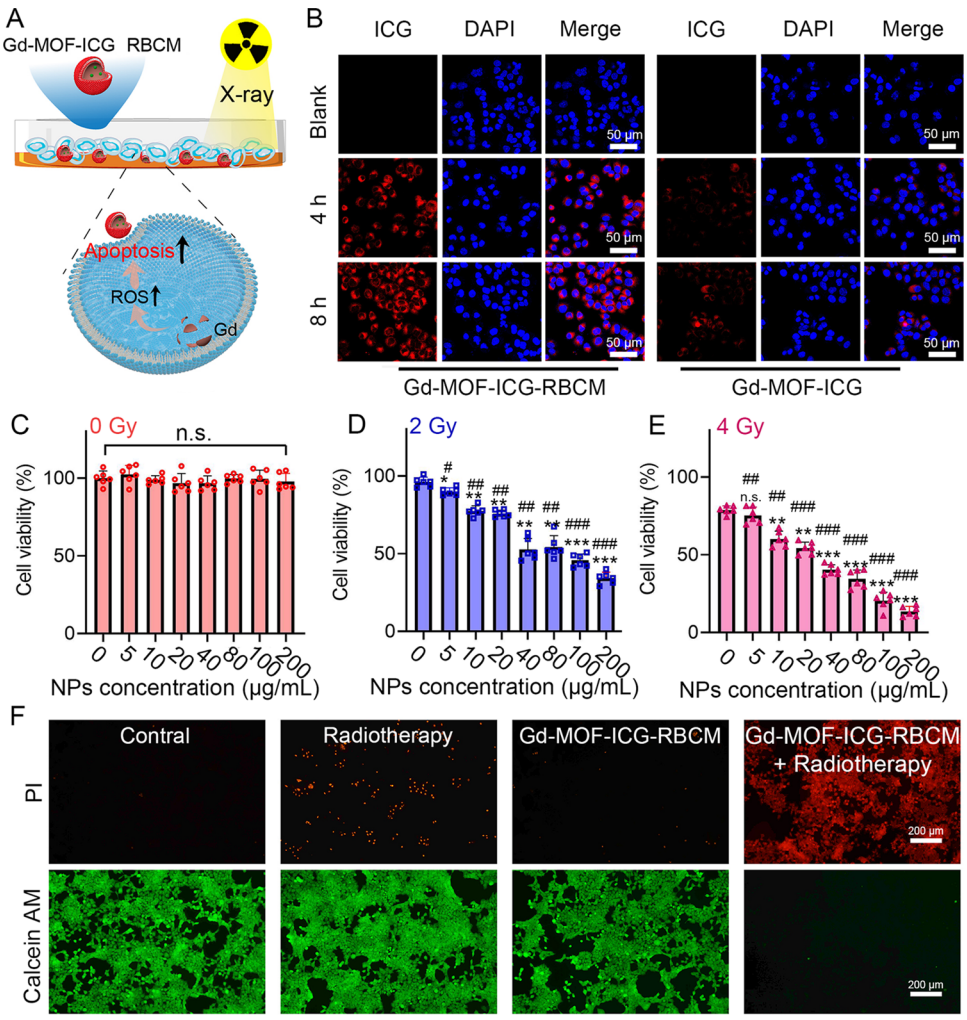

Figure 3. In vitro antitumor effects of Gd-MOF-ICG-RBCM. (A) Schematic representation of tumor cell destruction in vitro. (B) CLSM images of CNE1 cells after coincubation with Gd-MOF-ICG-RBCM and Gd-MOF-ICG at 4 and 8 h. CCK-8 viability assay of CNE1 cells treated with RT [(C) 0 Gy, (D) 2 Gy, and (E) 4 Gy] at various concentrations ($^{*}p < 0.05$, $^{**}p < 0.01$, $^{***}p < 0.001$, $n = 6$; $^{\#}p < 0.05$, $^{\#\#}p < 0.01$, $^{\#\#\#}p < 0.001$, comparison of 0 Gy in Figure 4C, $n = 5$). (F) Fluorescent imaging of the Live/dead staining assay (green for live cells; red for dead cells).

concentration of the radiosensitizer and the dose of radiotherapy, the number of apoptotic cells also increased. It is also clear from the figures that the radiotherapy group, which did not add nanoparticles, also had a significant killing effect. This indicates that the efficacy of radiotherapy urgently requires the addition of radiosensitizers. Next, to demonstrate the killing effect of Gd-MOF-ICG-RBCM on CNE1 cells, CNE1 cells treated with Gd-MOF-ICG-RBCM were irradiated with 0, 2, and 4 Gy of radiation. As shown in Figure 3D,E, under radiation, Gd-MOF-ICG-RBCM NPs exhibited dose-dependent cytotoxicity to CNE1 cancer cells, with cell viability dropping to 40% at an NPS concentration of 40 μg/mL under 4 Gy irradiation.

To further confirm the RT effect of Gd-MOF-ICG-RBCM, cells treated with it were stained with Calcein AM and propidium iodide (PI) to visually observe their survival status (Figure 3F). As shown in Figure S6, the expression of γ-H2AX (a DNA-damaging molecular protein) produced by radiotherapy corresponds to that of the live or dead staining. Compared with the control group, the cells, which were only incubated with Gd-MOF-ICG-RBCM, exhibited intact green fluorescence without cytotoxicity, indicating that the nanoparticles had no apparent toxicity and high biological safety. Cells that were only irradiated (4 Gy) also showed red cell killing effects, but after being incubated with NPs and then irradiated, most of the cells were killed. All of these indicate that the combination of nanoparticle incubation and X-ray irradiation showed a strong killing effect, suggesting that Gd-MOF-ICG-RBCM has great potential in NPC radiotherapy sensitization treatment.

2.4. In Vivo Fluorescence Imaging. Due to the colloidal stability of the nanomaterials in serum, Gd-MOF-ICG-RBCM may be applied for in vivo fluorescence imaging-guided radiotherapy. To study the in vivo EPR (enhanced permeability and retention) properties of this nanomaterial, we established a subcutaneous NPC tumor model, and the therapeutic plan is reflected in Figure 4A. The nanomaterials (10 mg/kg per mouse) were injected into the peripheral blood via tail vein injection, and through observing the live imaging fluorescence photos, we can see from Figure 4B that the nanomaterials coated with RBCM have good distribution in the body, and the in vivo circulation time is greatly extended, increasing the possibility of tumor uptake of nanomaterials. At the same time, we also found that Gd-MOF-ICG mainly has strong fluorescence signals around the intestines and kidneys after the injection of nanomaterials, while Gd-MOF-ICG-

https://doi.org/10.1021/acsomega.4c06191
ACS Omega 2024, 9, 38272−38283

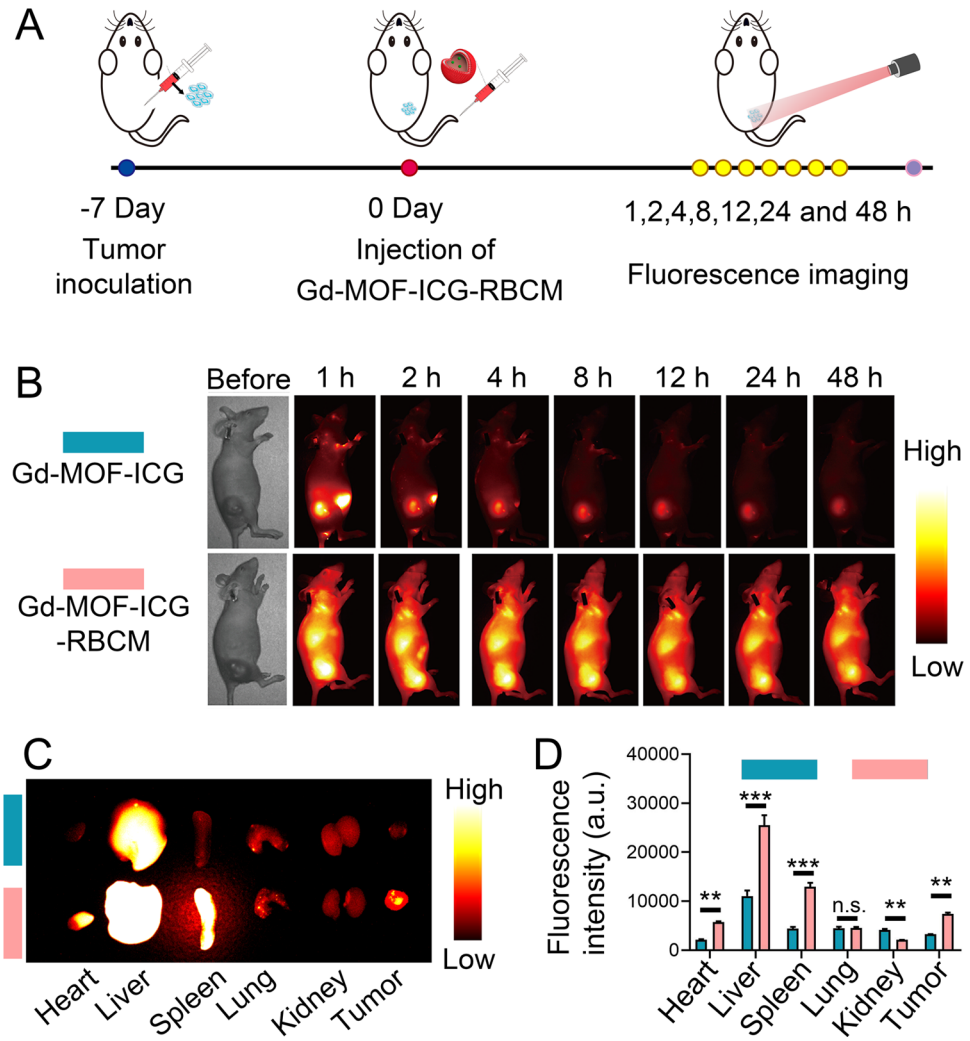

Figure 4. In vivo EPR effect of Gd-MOF-ICG-RBCM at the tumor site and its distribution in vivo observed by fluorescence images. (A) Schematic illustration of the timeline for fluorescence imaging of mice after intravenous injection of Gd-MOF-ICG-RBCM (10 mg/kg) at various time points. (B) In vivo fluorescence imaging of a mouse, which has a CNE1 tumor, captured at different time intervals following an intravenous injection. (C) Images depicting the fluorescence of major organs and the tumor in the mouse bearing the tumor, captured 48 h after administering Gd-MOF-ICG-RBCM (10 mg/kg). (D) Quantitative analysis of the major organs dissected from mice, conducted 48 h after the intravenous administration of Gd-MOF-ICG-RBCM (10 mg/kg) (*$p < 0.05$, **$p < 0.01$, ***$p < 0.001$; $n = 3$).

RBCM nanoparticles can be seen with significant fluorescence signals throughout the body, which is mainly due to the camouflage of RBCM which prevents the body from systematically clearing Gd-MOF-ICG-RBCM and thus excreting it from the body. Because live imaging cannot clearly observe the fluorescence content of the major organs, mice were euthanized at 48 h, and the major organs and tumors were extracted for imaging. Gd-MOF-ICG as the control group, from Figure 4C,D, it can be seen that the spleen has strong fluorescence in the Gd-MOF-ICG-RBCM group, this is due to the red blood cell homing effect, perfectly avoiding the mechanism of blood clearance of nanomaterials, resulting in more nanomaterials appearing in the spleen than in the control group. From the figure, we can also get some information: the tumor site fluorescence signal of the Gd-MOF-ICG-RBCM group is also significantly more than that of the Gd-MOF-ICG control group, which is due to the camouflage of the red blood cell membrane greatly increasing the in vivo circulation time of the nanomaterials, enhancing the EPR effect. This has increased the sensitivity for subsequent radiotherapy sensitization. Gd-MOF-ICG-RBCM nanoparticles are mainly located in the tumor tissue for over 48 h, highlighting the advantage of the stromal barrier in preventing nanoscale particles from circulating out of the tumor tissue.

2.5. In Vivo Radiotherapy. Next, the in vivo radiotherapy effect of Gd-MOF-ICG-RBCM nanoparticles was assessed, with the treatment schedule over time presented in Figure 5A,B. Mice were randomly assigned to four groups: an injection of PBS as a control group, radiotherapy alone (4 Gy × 3), Gd-MOF-ICG-RBCM, and Gd-MOF-ICG-RBCM + radiotherapy (4 Gy × 3, $n = 5$). As shown in Figure 5C, the volume of the tumor, which was recorded and summarized statistically, was compared on the 14th day. It was found that the tumors in the control group and the Gd-MOF-ICG-RBCM group grew rapidly, indicating that they had almost no effect or inhibitory action on tumor growth. The growth of tumors in the radiotherapy-alone group was restricted compared to the control group, suggesting that low-dose radiotherapy does not completely kill the tumor and lacks the ability to eradicate it. After the end of the tumor statistics, all mice were euthanized

https://doi.org/10.1021/acsomega.4c06191
ACS Omega 2024, 9, 38272−38283

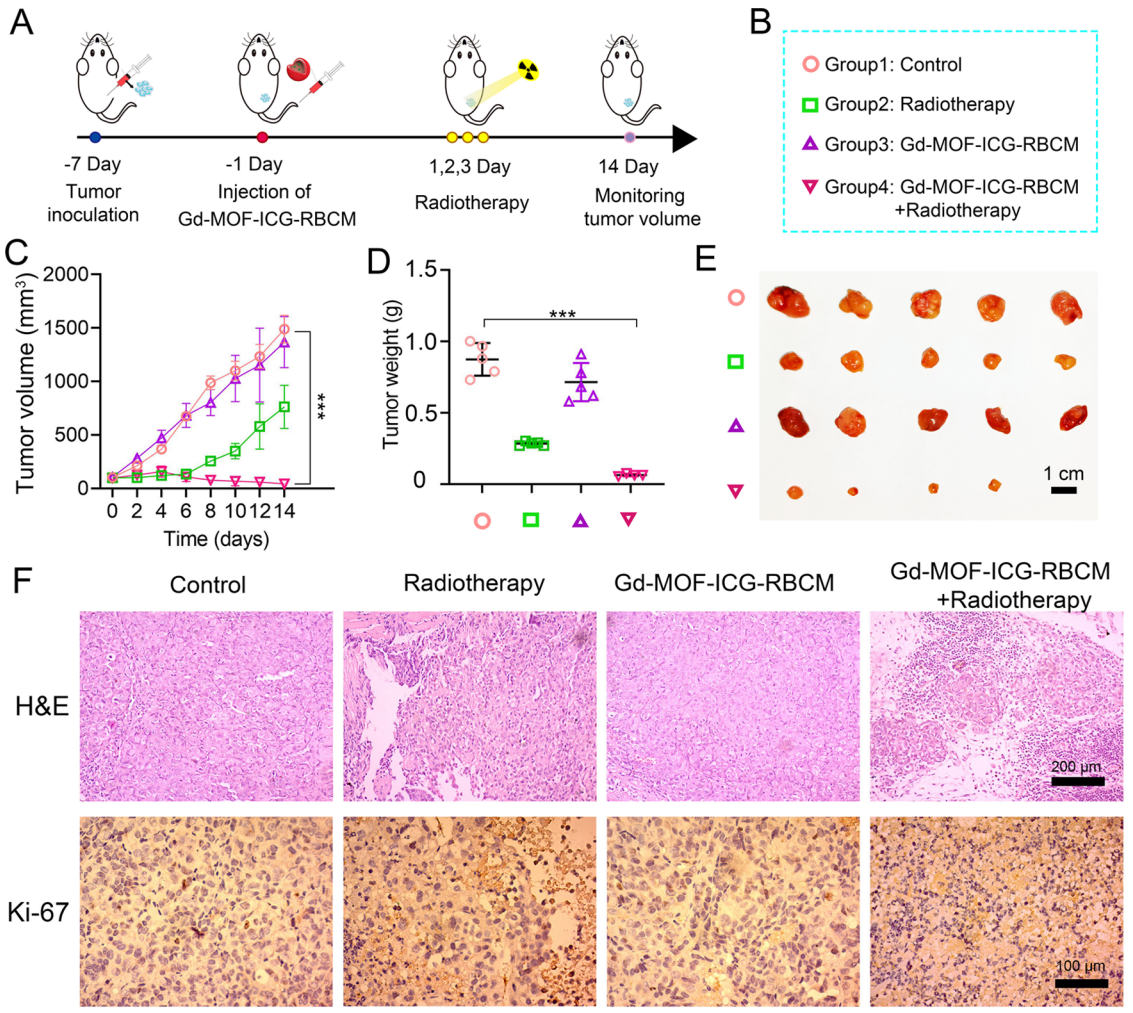

Figure 5. In vivo Gd-MOF-ICG-RBCM (10 mg/kg) injected intravenously, followed by X-ray irradiation (total: 12Gy, 3 day) in a unilateral CNE1 tumor model for the treatment of primary tumors. (A) Mouse treatment plan for imaging-guided radiotherapy sensitization therapy mediated by Gd-MOF-ICG-RBCM. (B) Schematic illustrations for each group's labeling. (C) Time-dependent growth curves of the tumors ($^{*}p < 0.05$, $^{**}p < 0.01$, $^{***}p < 0.001$, comparison of day 14 data; $^{\#}p < 0.05$, $^{\#\#}p < 0.01$, $^{\#\#\#}p < 0.001$, comparison of day 14 data, $n = 5$). (D) Average mass of ex vivo tumors from the four experimental groups ($^{*}p < 0.05$, $^{**}p < 0.01$, $^{***}p < 0.001$, compared to the PBS group; $n = 5$). (E) Photographs of ex vivo tumors from the four experimental groups. (F) H&E staining and Ki67 immunohistochemistry of tumor sections from each group.

by cervical dislocation, and the tumor mass and pictures from each treatment group, as shown in Figure 5D,E, were obtained. It can be observed that the growth trends of tumors in each group were consistent with the changes in tumor volume over time, all indicating that Gd-MOF-ICG-RBCM has a radiosensitizing effect. After the photo weighing was finished, the tumors, which were extracted, underwent slice analysis for H&E staining. The effect of radiotherapy on solid tumors was amplified by Gd-MOF-ICG-RBCM, as can be seen from Figure 5F in Group 4, where the damage to the tumor tissue was the most severe with apparent apoptosis and nuclear shrinkage observed. The tumor cells in the control group and the Gd-MOF-ICG-RBCM group appeared to be in good condition. Simultaneously, Antigen K_i-67 immunohistochemical testing also showed that the combination of Gd-MOF-ICG-RBCM nanoprobes and radiotherapy led to extensive apoptosis within the cells.

The risk of systemic side effects is an important factor limiting the clinical application of Gd-MOF-ICG-RBCM. To evaluate the in vivo toxicity of the nanoprobe, the main organs from each treatment group, which were obtained, underwent H&E staining, as shown in Figure S7. We further collected blood from mice 12 days post-treatment for complete blood count and serum biochemical analysis, and it can be observed that there were no significant differences in the mice after injection (Figures S8 and S9). The H&E staining of the main organs (heart, liver, spleen, lungs, and kidneys) revealed no obvious inflammatory responses or damage such as necrosis during the treatment process, indicating that the radiosensitizer has good biocompatibility in the body. As shown in Figures S10 and S11, the hemolysis experiment evaluated the hemolytic effect of different concentrations of the Gd-MOF-ICG-RBCM solution on red blood cells. The specific experimental results are as follows: The hemolysis rates for all concentrations of the Gd-MOF-ICG-RBCM solution did not exceed the 5% hemolysis threshold, which is considered the critical value for safety when compared to the negative control group.

As can be seen from Figure S12, the body weight of the mice in each group steadily increased with no significant changes in body weight during the administration period in any of the

https://doi.org/10.1021/acsomega.4c06191
ACS Omega 2024, 9, 38272−38283

groups, suggesting that Gd-MOF-ICG-RBCM has good biocompatibility.

In our study, we utilized CNE1 cells, which have low radiosensitivity. This choice underscores our objective to tackle radioresistance, a prevalent issue in NPC treatment. Our engineered material demonstrates a significant capacity to enhance the radiosensitivity of these cells. By facilitating targeted delivery and prolonged tumor site retention, it markedly improves radiotherapy outcomes for NPC. This breakthrough suggests our material's potential to reduce necessary radiation doses, minimizing adverse effects and offering a promising avenue for enhancing NPC treatment efficacy.

3. CONCLUSIONS

We have developed a strategy that facilitates radiotherapy positioning, synthesizing nanoparticles Gd-MOF-ICG-RBCM, which are conducive to realizing precise radiosensitization of tumors and have an approximate diameter of 100 nm. These nanoprobes, with their long blood circulation time, are suitable for passive tumor targeting, possessing excellent biosafety and anticancer activity. After circulating through the blood, the nanomaterials enter the tumor and, guided precisely by near-infrared second-window fluorescence imaging, direct X-ray irradiation to the subcutaneous tumor. The ROS produced by the Gd element in the nanoprobe significantly enhances the effect of radiotherapy. Ultimately, this achieves a treatment that is both precise and efficient with low side effects.

As a result, the use of low doses of X-rays can realize the radiosensitization effect of Gd-MOF-ICG-RBCM, significantly inhibiting the growth of subcutaneous tumors. Therefore, Gd-MOF-ICG-RBCM nanoparticles disguised by red blood cells can extend the circulation time in the body and increase the retention effect of tumors on the nanomaterials. Using near-infrared second-window fluorescence imaging to precisely guide radiosensitization of solid tumors has promising applications. The strategy of second-window fluorescence imaging-guided radiotherapy that we propose offers a new strategy and methods for accurately treating NPC in clinical settings.

4. EXPERIMENTAL SECTION

4.1. Materials and Reagents. Gadolinium nitrate hexahydrate, iron (III chloride hexahydrate), and 1,3,5-benzenetricarboxylic acid were purchased from China National Pharmaceutical Group Chemical Reagent Co., Ltd. Fumaric acid and *N*,*N*-dimethylformamide were acquired from Sigma-Aldrich Co., Ltd. 3-(2-Octyl-dodecyl)-thiophene was sourced from Derthon OPV Co Ltd. Dio, DAPI, and CCK-8 were provided by Dojindo Molecular Technologies. The Viability/Cytotoxicity Kit and K_i-67 antibody were purchased from Invitrogen. DCFH-DA and ABDA were obtained from Beyotime.

4.2. Cell Culture and Animals. The CNE1 cells (nasopharyngeal carcinoma cells) were obtained from ATCC. These cells were cultured at 37 °C in a humidified atmosphere with 5% CO_2 using a medium containing 10% fetal bovine serum (FBS) and 1% penicillin-streptomycin.

For in vivo studies, male nude mice (6 and 8 weeks old) were purchased from the Shanghai Wushi Lab. Animal Research Center (Shanghai, China). All animal experiments were conducted with the approval of the Institutional Animal Care and Use Committee at First Affiliated Hospital of Fujian Medical University.

4.3. Apparatus and Characterization. The UV−visible (UV−vis) absorption spectra were obtained by using a Synergy Neo2 HTS microplate reader. The high-pressure reaction vessel was supplied by Lindberg/Blue M.

The particle size distribution and ζ-potential were determined using a Malvern Zeta sizer Nano ZS dynamic light scattering instrument. Distilled water with a conductivity of 18.2 MΩ/cm was purified using the Ultrapure and Pure Water Purification System (Milli-Q IQ 7003/05/10/15). To observe the size and morphology of the nanoparticles, transmission electron microscopy (TEM) was conducted with a JEOL JEM-2100 instrument. Cellular fluorescence imaging was performed by using a Zeiss LSM 780 confocal laser scanning microscope and a Nikon ECLIPSE Ti2 fluorescence microscope. The crystalline structures of the nanoparticles were analyzed by using a Rigaku D8-advance X-ray diffraction system in Japan. X-rays were obtained from a Thermo Scientific Escalab 250Xi irradiator. In vivo fluorescence imaging of small animals was conducted using a homemade multispectral photoacoustic microscopy system.

4.4. Preparation of Gd-MOF-ICG. This passage describes the method of preparing Gd/FeMOF nanospheres using a solvothermal approach. In brief, 4.1 mg of gadolinium nitrate hexahydrate ($Gd(NO_3)_3{\cdot}6H_2O$), 2.4 mg of iron(III) chloride hexahydrate ($FeCl_3{\cdot}6H_2O$), 1.9 mg of 1,3,5-benzenetricarboxylic acid (H_3BTC), and 3.6 mg of fumaric acid were dissolved in 60 mL of *N*,*N*-dimethylformamide (DMF). After the solution was thoroughly mixed, it was transferred into a Teflon-lined stainless-steel autoclave and heated at 120 °C for 4 h. The resulting product was collected via centrifugation and then washed 3 times with ethanol. The precipitate, which had been redispersed in 5 mL of distilled water by using an ultrasonic instrument, was set aside. A dimethyl sulfoxide (DMSO) solution containing 1.2 mg of ICG was mixed and stirred with the 5 mL nanoparticle dispersion system for 24 h, resulting in the isolation of Gd-MOF-ICG through centrifugation.

4.5. Extraction of Red Blood Cell Membrane (RBCM). Red blood cells were extracted from the orbital cavity of the mice. Initially, the blood was placed in a container containing an anticoagulant, and a low-speed centrifugation method was employed to separate the red blood cells from the blood, followed by repeated washing with an isotonic buffer to remove the plasma. In the second step, the washed red blood cells were transferred from the isotonic buffer to a hypotonic buffer. In the final step, the lysed red blood cells were thoroughly and repeatedly washed through high-speed centrifugation to remove hemoglobin and other intracellular contents. This process resulted in the preparation of the final product, the red blood cell membrane. A portion of the red blood cell membrane solution was taken and freeze-dried for quantification.

4.6. Preparation of Gd-MOF-ICG-RBCM. The encapsulation of RBCM around nanomaterials through a membrane extruder is carried out following the following specific steps: First, 1 mL of red blood cell membrane (0.5 mg/mL) is dispersed in 0.5 mL of distilled water containing 1 mg of nanoparticles using an ultrasonic disruptor. Subsequently, this solution is incubated in a 37 °C water bath for 30 min. Then, the solution is sequentially extruded through a liposome extruder (LiposoEasy LE-1) with pore sizes of 800, 400, and

https://doi.org/10.1021/acsomega.4c06191
ACS Omega 2024, 9, 38272−38283

200 nm. Finally, Gd-MOF-ICG-RBCM is obtained for further use.

4.7. ROS Quantification with the DPBF Assay. The solutions containing DPBF (at a working concentration of 50 μg/mL) were subjected to different doses of X-ray irradiation (0 and 4 Gy) in Gd-MOF-ICG-RBCM solutions at various concentrations (20, 40, 60, 80 μg/mL). After irradiation, the absorbance intensity of the DPBF solution was measured to analyze changes in the peak of the DPBF.

4.8. ROS Quantification with the DCFH-DA Assay. The monitoring of intracellular ROS (reactive oxygen species) production is conducted using 2′,7′-dichlorofluorescin diacetate (DCFH-DA) as an indicator. Initially, CNE1 cells are cultured in a 96-well plate for 24 h with 8000 cells per well. Then, the cells are incubated with Gd-MOF-ICG-RBCM for 4 h and subsequently with the DCFH-DA probe for 30 min. Following this, the cells are subjected to 4 Gy of X-ray irradiation. Immediately, the fluorescent images of the cells' DCF are obtained through a fluorescence microscope.

4.9. Cell Uptake Analysis. The cellular uptake of Gd-MOF-ICG-RBCM was observed and quantitatively analyzed by using laser confocal fluorescence microscopy. A total of 1×10^5 CNE1 cells were cultured in 20 mm glass-bottom culture dishes for 24 h. Subsequently, the cells were coincubated with DiO-labeled Gd-MOF-ICG-RBCM (50 μg/mL) at different time points (2, 4, 6, and 8 h), with cells not exposed to nanoparticles serving as the control group. Following this, the cells in each culture dish were fixed with a 4% cell fixation solution. Prior to observation using confocal laser scanning microscopy (CLSM, LSM 780), they were stained with DAPI (1 μg/mL) for 15 min. Simultaneously, Gd-MOF-ICG-PEG was used as another matched group in the experiments.

4.10. CCK-8 and Cell Apoptosis Assay. Cell viability was assessed via the CCK-8 assay. A total of 1×10^4 of CNE1 cells were seeded in each well of 96-well plates for 24 h to ensure cell attachment. Subsequently, the cells were treated with varying concentrations of Gd-MOF-ICG-RBCM (0, 1, 2, 4, 8, 16, 32, 64, 96, and 128 μg/mL). After 4 h of incubation, the cells were exposed to different doses of X-ray radiation (0, 4, and 8 Gy). Following irradiation, the cells were further cultured for 48 h, and cell viability was determined using the CCK-8 assay. The absorbance of each well was measured at a wavelength of 450 nm using a microplate reader (Spectra Max M5).

Simultaneously, cell viability was also assessed using live/dead viability/cytotoxicity kit staining (Calcein AM) with a concentration of 64 μg/mL of the nanomaterial and different radiation doses (4 and 8 Gy). Fluorescent images were acquired and observed by using a fluorescence microscope.

4.11. In Vitro Generation of ROS. In vitro generation of ROS commenced with the creation of Gd-MOF-ICG-RBCM nanoparticle solutions at specified concentrations (0, 10, 20, 40, 50, 100, and 200 μg/mL). These solutions were then concurrently treated in two distinct protocols. The first protocol involved mixing with 1,3-diphenylisobenzofuran (DPBF) to target ROS detection. In parallel, the second protocol entailed incubation with cells previously treated with 2′, 7′-dichlorofluorescein diacetate (DCFH-DA) for intracellular ROS identification. Solutions without nanoparticles served as negative controls, in contrast to a designated ROS generator acting as the positive control. Upon X-ray irradiation at 4 Gy, the DPBF solution underwent absorption monitoring at 410 nm to evaluate $^1O_2$ generation, whereas fluorescence microscopy facilitated the observation of DCF fluorescence, indicating the ROS levels within the cells. Conducted at 37 °C, these steps delineated the concentration-dependent ROS production capability of Gd-MOF-ICG-RBCM, thereby underlining its utility in amplifying radiotherapy's cytotoxic impact via enhanced oxidative stress in tumor cells.

4.12. Hemolysis Assay. First, 1 mL of blood was collected from the eyeballs of the Nude mouse. Subsequently, RBCs were obtained by centrifugation at 1000*g* for 10 min. Then, the RBCs were resuspended in 5 mL of PBS along with 2 mL of Gd-MOF-ICG-RBCM at different concentrations (0, 10, 20, 40, 50, 100, and 200 μg/mL). The RBCs resuspended in PBS without any further treatment were used as negative control. RBCs resuspended in a 1% Triton X-100 solution were used as the positive control. Subsequently, each mixture was incubated for 2 h on a shaker (100 rpm, 37 °C), followed by centrifugation at 3000 rpm for 10 min to remove intact RBCs and cell debris. Finally, the absorbance of the supernatants was measured by using a microplate reader at a wavelength of 540 nm to calculate the hemolysis rate.

4.13. Biodistribution and Fluorescence Imaging In Vivo. Tumor-bearing mice were established by the subcutaneous injection of a suspension of CNE1 cells. Nude mice (6−8 weeks) were subcutaneously injected with a CNE1 cell suspension (25×10^4 cells, diluted in 25 μL PBS) in the right hip. When the tumor volume reached approximately 200 mm^3 (tumor volume calculated using the formula $L \times W \times W/2$), Gd-MOF-ICG-RBCM (nanomaterial equivalent of 10 mg/kg) and Gd-MOF-ICG (10 mg/kg) were intravenously injected into the mice's bloodstream. Imaging was performed 0, 1, 2, 4, 8, 12, 24, and 48 h after administration using a near-infrared imaging system. The excitation wavelength was 785 nm, and the fluorescence emission signal was collected at 810 nm. Finally, at 48 h, organs such as the mouse's heart, liver, spleen, lung, kidney, and tumors were collected. Fluorescence imaging was then performed. After the fluorescence images were obtained, fluorescence quantitative analysis was conducted.

4.14. Radiotherapy In Vivo. Tumor-bearing mice were established by subcutaneous injection of a suspension of CNE1 cells. Nude mice aged 6−8 weeks were subcutaneously injected with a CNE1 cell suspension (25×10^4 cells, diluted in 25 μL of PBS) into the subcutaneous tissue of the right hip. And then the mice were divided into 4 groups, each consisting of 5 mice. The groups were as follows: PBS, PBS + RT, Gd-MOF-ICG-RBCM, and Gd-MOF-ICG-RBCM + RT. When the tumor volume reached approximately 100 mm^3, PBS (100 μL of the same volume) or Gd-MOF-ICG-RBCM (10 mg/kg) was intravenously injected into the mice. Subsequently, the mice's tumors were irradiated with X-rays at 24, 48, and 72 h. The mice were anesthetized using a 1% pentobarbital sodium solution, and the radiation dose was 4 Gy.

Afterward, the mice's body weight and tumor volume were recorded every 2 days. Tumor volume was calculated using the formula $V = (a \times b^2)/2$, where "a" and "b" represent the length and width of the tumor, respectively. After 14 days, the mice were euthanized, and their major organs and tumors were harvested. Tumor samples were then fixed in formalin and subjected to H&E staining and immunohistochemical analysis for K_i-67 expression. Finally, H&E staining analysis was also performed on the harvested organs.

4.15. Method for Assessing DNA Damage Using High-Resolution Confocal Immunofluorescence Imaging. To visualize and assess the DNA damage protein γ-H2AX

https://doi.org/10.1021/acsomega.4c06191
ACS Omega 2024, 9, 38272−38283

in cells under different treatment conditions, we employed high-resolution confocal microscopy (shown in Figure S6). Cells were cultured in appropriate dishes until they reached the desired confluency and then divided into four groups: Control, Radiotherapy only, Gd-MOF-DiO-RBCM only, and Gd-MOF-DiO-RBCM with Radiotherapy. The radiotherapy groups were treated with the specified radiation dose, and cells were incubated with Gd-MOF-DiO-RBCM or DiO dye as required. Following treatment, cells were fixed with 4% paraformaldehyde for 15 min at room temperature and washed 3 times with PBS. Cells were then permeabilized with 0.1% Triton X-100 in PBS for 10 min, followed by three washes with PBS. Nonspecific binding sites were blocked with 1% BSA in PBS for 30 min at room temperature. Cells were incubated with γ-H2AX primary antibody (specific dilution) overnight at 4 °C. After washing 3 times with PBS, cells were incubated with the secondary antibody conjugated with a fluorescent dye (specific dilution) for 1 h at room temperature in the dark. Nuclear staining was performed using DAPI (specific dilution) for 5 min at room temperature in the dark, followed by three washes with PBS. Cells were then mounted with an appropriate mounting medium and images were acquired using a high-resolution confocal microscope (specific model). Images were captured at different channels for DAPI and γ-H2AX to observe nuclear morphology and DNA damage, respectively. The images were merged to visualize the colocalization of γ-H2AX with the cell nuclei, and further analyzed using appropriate software to quantify DNA damage across different treatment groups. Consistent imaging settings were maintained across all samples to ensure accurate comparison, and all experimental conditions were thoroughly documented for reproducibility.

4.16. Method for X-ray Diffraction (XRD) Analysis. To characterize the crystalline structure of Gd-MOF-ICG-RBCM nanomaterials, we performed X-ray diffraction (XRD) analysis. The Gd-MOF-ICG-RBCM samples were prepared and dried to obtain a fine powder. The XRD patterns were recorded using a diffractometer equipped with a Cu Kα radiation source (wavelength = 1.5406 Å). The samples were scanned over a 2θ range from 10 to 70° at a step size of 0.02° and a scanning speed of 2° per minute. The intensity of the diffracted X-rays was measured and plotted against the diffraction angle (2θ) to obtain the XRD patterns. The resulting diffraction pattern, shown in Figure S6, was analyzed to identify the crystalline phases present in the sample and to assess the material's crystallinity. The peaks observed in the XRD pattern correspond to the specific planes of the crystalline structure, confirming the successful synthesis of Gd-MOF-ICG-RBCM nanomaterials.

4.17. Blood Biochemistry Analysis. Mice were injected with either PBS or Gd-MOF-ICG-RBCM. After 12 days, the blood was collected from the orbital sinus. One portion of the blood was immediately placed into a centrifuge tube containing a coagulant and allowed to stand at room temperature for 30−60 min. The sample was then centrifuged at 1000*g* relative centrifugal force (RCF) for 10 min. The separated serum was carefully pipetted into a clean centrifuge tube for analysis using an automated biochemical analyzer (SIEMENS/ADVIA XPT).

Another portion of the blood was mixed thoroughly with an anticoagulant immediately upon collection. This sample was used for complete blood count (CBC) analysis with an automated hematology analyzer (ADVIA 2120i/Siemens).

4.18. Statistical Analysis. Using the Student's *t* test, the significance within the two groups was determined. $^{*}P < 0.05$, $^{**}P < 0.01$, and $^{***}P < 0.001$, and the results were expressed as mean ± SD.

■ ASSOCIATED CONTENT

Supporting Information

The Supporting Information is available free of charge at https://pubs.acs.org/doi/10.1021/acsomega.4c06191.

XRD patterns of Gd-MOF-ICG-RBCM (Figure S1); flow cytometry analysis of intracellular ROS generation (Figure S2); CLSM images of CNE1 cells after coincubation with Gd-MOF-DiO-RBCM and Gd-MOF-DiO at 2, 4, 6, and 8 h (Figure S3); flow cytometry data on the cellular uptake of Gd-MOF-ICG-RBCM (Figure S4); flow cytometry data on the cellular uptake of Gd-MOF-ICG (Figure S5); high-resolution confocal immunofluorescence images showing the DNA damage protein γ-H2AX (Figure S6); H&E staining of major organs (heart, liver, spleen, lung, kidney) in different groups demonstrating the safety of the material (Figure S7); blood biochemical index of liver and kidney function markers 12 days after intravenous injection with PBS and Gd-MOF-ICG-RBCM (Figure S8); blood routine analysis 12 days after intravenous injection with PBS and Gd-MOF-ICG-RBCM (Figure S9); hemolysis experiment with different Gd-MOF-ICG-RBCM concentrations (Figure S10); hemolysis rate of Gd-MOF-ICG-RBCM at different concentrations (Figure S11); and body weight changes in animals during treatment in different groups (Figure S12) (PDF)

■ AUTHOR INFORMATION

Corresponding Author

Xi Zou − *Department of Radiotherapy, Cancer Center, The First Affiliated Hospital of Fujian Medical University, Fuzhou 350005, China; Department of Radiotherapy, National Regional Medical Center, Binhai Campus of the First Affiliated Hospital, Fujian Medical University, Fuzhou 350212, China; Key Laboratory of Radiation Biology of Fujian Higher Education Institutions, The First Affiliated Hospital, Fujian Medical University, Fuzhou 350212, China;* orcid.org/0000-0001-6530-6076; Email: zouxi505@163.com

Authors

Wenlong Lv − *Department of Radiotherapy, Cancer Center, The First Affiliated Hospital of Fujian Medical University, Fuzhou 350005, China; Department of Radiotherapy, National Regional Medical Center, Binhai Campus of the First Affiliated Hospital, Fujian Medical University, Fuzhou 350212, China; Key Laboratory of Radiation Biology of Fujian Higher Education Institutions, The First Affiliated Hospital, Fujian Medical University, Fuzhou 350212, China*

Yanbin Chen − *Department of Radiotherapy, Cancer Center, The First Affiliated Hospital of Fujian Medical University, Fuzhou 350005, China; Department of Radiotherapy, National Regional Medical Center, Binhai Campus of the First Affiliated Hospital, Fujian Medical University, Fuzhou 350212, China*

Wencong Hong − *Department of Comprehensive Oncology, The Hospital of Nanan City, Nanan 362300, China*

https://doi.org/10.1021/acsomega.4c06191
ACS Omega 2024, 9, 38272−38283

Linzhen Lan − *Department of Radiotherapy, Cancer Center, The First Affiliated Hospital of Fujian Medical University, Fuzhou 350005, China; Department of Radiotherapy, National Regional Medical Center, Binhai Campus of the First Affiliated Hospital, Fujian Medical University, Fuzhou 350212, China*

Jun Chen − *Department of Radiotherapy, Cancer Center, The First Affiliated Hospital of Fujian Medical University, Fuzhou 350005, China; Department of Radiotherapy, National Regional Medical Center, Binhai Campus of the First Affiliated Hospital, Fujian Medical University, Fuzhou 350212, China*

Feibao Guo − *Department of Radiotherapy, Cancer Center, The First Affiliated Hospital of Fujian Medical University, Fuzhou 350005, China; Department of Radiotherapy, National Regional Medical Center, Binhai Campus of the First Affiliated Hospital, Fujian Medical University, Fuzhou 350212, China; Key Laboratory of Radiation Biology of Fujian Higher Education Institutions, The First Affiliated Hospital, Fujian Medical University, Fuzhou 350212, China*

Complete contact information is available at: https://pubs.acs.org/10.1021/acsomega.4c06191

Author Contributions

[⊥]W.L. and Y.C. contributed equally to this work.

Notes

The authors declare no competing financial interest.

■ ACKNOWLEDGMENTS

The authors are grateful for the economic support from the Natural Science Foundation of Fujian Province (General Program, Grant Number: 2022J01220), Startup Fund for scientific research, Fujian Medical University (Grant number: 2021QH1087)

■ REFERENCES

(1) Tang, L. L.; Chen, Y. P.; Chen, C. B.; Chen, M. Y.; Chen, N. Y.; Chen, X. Z.; Du, X. J.; Fang, W. F.; Feng, M.; Gao, J.; et al. The Chinese Society of Clinical Oncology (CSCO) clinical guidelines for the diagnosis and treatment of nasopharyngeal carcinoma. *Cancer Commun.* **2021**, *41* (11), 1195−1227.

(2) Chen, W.; Zheng, R.; Baade, P. D.; Zhang, S.; Zeng, H.; Bray, F.; Jemal, A.; Yu, X. Q.; He, J. Cancer statistics in China, 2015. *CA Cancer J. Clin.* **2016**, *66* (2), 115−132.

(3) Du, J.; Gu, Z.; Yan, L.; Yong, Y.; Yi, X.; Zhang, X.; Liu, J.; Wu, R.; Ge, C.; Chen, C.; et al. Poly(Vinylpyrollidone)- and Selenocysteine-Modified Bi(2) Se(3) Nanoparticles Enhance Radiotherapy Efficacy in Tumors and Promote Radioprotection in Normal Tissues. *Adv. Mater.* **2017**, *29* (34), No. 1701268. Chan, L.; Gao, P.; Zhou, W.; Mei, C.; Huang, Y.; Yu, X. F.; Chu, P. K.; Chen, T. Sequentially Triggered Delivery System of Black Phosphorus Quantum Dots with Surface Charge-Switching Ability for Precise Tumor Radiosensitization. *ACS Nano* **2018**, *12* (12), 12401−12415. Lu, Z.; Zheng, X.; Ding, C.; Zou, Z.; Liang, Y.; Zhou, Y.; Li, X. Deciphering the Biological Effects of Radiotherapy in Cancer Cells. *Biomolecules* **2022**, *12* (9), No. 1167.

(4) Li, H. L.; Deng, N. H.; Xiao, J. X.; He, X. S. Cross-link between ferroptosis and nasopharyngeal carcinoma: New approach to radiotherapy sensitization. *Oncol. Lett.* **2021**, *22* (5), 770−780.

(5) Ni, K.; Lan, G.; Chan, C.; Quigley, B.; Lu, K.; Aung, T.; Guo, N.; La Riviere, P.; Weichselbaum, R. R.; Lin, W. Nanoscale metal-organic frameworks enhance radiotherapy to potentiate checkpoint blockade immunotherapy. *Nat. Commun.* **2018**, *9* (1), No. 2351.

(6) Li, Y.; Yang, J.; Gu, G.; Guo, X.; He, C.; Sun, J.; Zou, H.; Wang, H.; Liu, S.; Li, X.; et al. Pulmonary Delivery of Theranostic Nanoclusters for Lung Cancer Ferroptosis with Enhanced Chemodynamic/Radiation Synergistic Therapy. *Nano Lett.* **2022**, *22* (3), 963−972.

(7) Du, Z.; Wang, X.; Zhang, X.; Gu, Z.; Fu, X.; Gan, S.; Fu, T.; Xie, S.; Tan, W. X-Ray-triggered Carbon Monoxide and Manganese Dioxide Generation based on Scintillating Nanoparticles for Cascade Cancer Radiosensitization. *Angew. Chem., Int. Ed.* **2023**, *62* (23), No. e202302525.

(8) Li, J.; Hu, Y.; Yang, J.; Wei, P.; Sun, W.; Shen, M.; Zhang, G.; Shi, X. Hyaluronic acid-modified Fe3O4@Au core/shell nanostars for multimodal imaging and photothermal therapy of tumors. *Biomaterials* **2015**, *38*, 10−21.

(9) Yon, M.; Billotey, C.; Marty, J. D. Gadolinium-based contrast agents: From gadolinium complexes to colloidal systems. *Int. J. Pharm.* **2019**, *569*, No. 118577.

(10) Abbasi, A. R.; Rizvandi, M.; Azadbakht, A.; Rostamnia, S. Controlled uptake and release of imatinib from ultrasound nanoparticles Cu3(BTC)2 metal-organic framework in comparison with bulk structure. *J. Colloid Interface Sci.* **2016**, *471*, 112−117. Li, Z.; Lai, M.; Zhao, S.; Zhou, Y.; Luo, J.; Hao, Y.; Xie, L.; Wang, Y.; Yan, F. Ultrasound Molecular Imaging for Multiple Biomarkers by Serial Collapse of Targeting Microbubbles with Distinct Acoustic Pressures. *Small* **2022**, *18* (22), No. e2108040.

(11) Huang, D.; Wang, Q.; Cao, Y.; Yang, H.; Li, M.; Wu, F.; Zhang, Y.; Chen, G.; Wang, Q. Multiscale NIR-II Imaging-Guided Brain-Targeted Drug Delivery Using Engineered Cell Membrane Nanoformulation for Alzheimer's Disease Therapy. *ACS Nano* **2023**, *17* (5), 5033−5046.

(12) Zu, Y.; Wang, Z.; Yao, H.; Yan, L. Oxygen-generating biocatalytic nanomaterials for tumor hypoxia relief in cancer radiotherapy. *J. Mater. Chem. B* **2023**, *11* (14), 3071−3088.

(13) Tang, R.; Yin, J.; Liu, Y.; Xue, J. FLASH radiotherapy: A new milestone in the field of cancer radiotherapy. *Cancer Lett.* **2024**, *587*, No. 216651.

(14) Chen, M.; Fu, Y.; Liu, Y.; Zhang, B.; Song, X.; Chen, X.; Zhu, Z.; Gao, H.; Yang, J.; Shi, X. NIR-Light-Triggered Mild-Temperature Hyperthermia to Overcome the Cascade Cisplatin Resistance for Improved Resistant Tumor Therapy. *Adv. Healthcare Mater.* **2024**, *13*, No. e2303667.

(15) Wang, D.; Nie, T.; Huang, C.; Chen, Z.; Ma, X.; Fang, W.; Huang, Y.; Luo, L.; Xiao, Z. Metal-Cyclic Dinucleotide Nanomodulator-Stimulated STING Signaling for Strengthened Radioimmunotherapy of Large Tumor. *Small* **2022**, *18* (41), No. e2203227.

(16) Carconi, C.; Cerreti, M.; Roberto, M.; Arrivi, G.; D'Ambrosio, G.; De Felice, F.; Di Civita, M. A.; Iafrate, F.; Lucatelli, P.; Magliocca, F. M.; et al. The management of oligometastatic disease in colorectal cancer: Present strategies and future perspectives. *Crit. Rev. Oncol. Hematol.* **2023**, *186*, No. 103990.

(17) Sun, L.-L.; Li, Y.-H.; Shi, H. A Ketone Functionalized Gd(III)-MOF with Low Cytotoxicity for Anti-Cancer Drug Delivery and Inhibiting Human Liver Cancer Cells. *J. Cluster Sci.* **2019**, *30* (1), 251−258.

(18) Chen, X.; Li, M.; Lin, M.; Lu, C.; Kumar, A.; Pan, Y.; Liu, J.; Peng, Y. Current and promising applications of Hf(iv)-based MOFs in clinical cancer therapy. *J. Mater. Chem. B* **2023**, *11* (25), 5693−5714.

(19) Cheng, Y.; Wen, C.; Sun, Y. Q.; Yu, H.; Yin, X. B. Mixed-Metal MOF-Derived Hollow Porous Nanocomposite for Trimodality Imaging Guided Reactive Oxygen Species-Augmented Synergistic Therapy. *Adv. Funct. Mater.* **2021**, *31* (37), No. 2104378.

(20) Chen, M.; Huang, X.; Lai, J.; Ma, L.; Chen, T. Substituent-regulated highly X-ray sensitive Os(VI) nitrido complex for low-toxicity radiotherapy. *Chin. Chem. Lett.* **2021**, *32* (1), 158−161.

(21) Li, J.; Wei, Z.; Lin, X.; Zheng, D.; Wu, M.; Liu, X.; Liu, J. Programmable Therapeutic Nanodevices with Circular Amplification of H2 O2 in the Tumor Microenvironment for Synergistic Cancer Therapy. *Adv. Healthcare Mater.* **2019**, *8* (10), No. e1801627.

(22) Wu, M. X.; Yang, Y. W. Metal-Organic Framework (MOF)-Based Drug/Cargo Delivery and Cancer Therapy. *Adv. Mater.* **2017**, *29* (23), No. 1606134.

(23) Zhou, W.; Liu, Z.; Wang, N.; Chen, X.; Sun, X.; Cheng, Y. Hafnium-Based Metal−Organic Framework Nanoparticles as a Radiosensitizer to Improve Radiotherapy Efficacy in Esophageal Cancer. *ACS Omega* **2022**, *7* (14), 12021−12029.
(24) Pu, K.; Shuhendler, A. J.; Jokerst, J. V.; Mei, J.; Gambhir, S. S.; Bao, Z.; Rao, J. Semiconducting polymer nanoparticles as photoacoustic molecular imaging probes in living mice. *Nat. Nanotechnol.* **2014**, *9* (3), 233−239.

https://doi.org/10.1021/acsomega.4c06191
ACS Omega 2024, 9, 38272−38283